Effect of Mesoscale Eddies on the Taiwan Strait Current

YU-LIN CHANG

National Taiwan Normal University, Taipei, Taiwan

YASUMASA MIYAZAWA

Japan Agency for Marine-Earth Science and Technology, Yokohama, Kanagawa, Japan

XINYU GUO

Ehime University, Matsuyama, Ehime, Japan

(Manuscript received 10 December 2014, in final form 22 March 2015)

ABSTRACT

This study shows that mesoscale eddies can alter the Taiwan Strait Current. The 20-yr data-assimilated Japan Coastal Ocean Predictability Experiment 2 (JCOPE2) reanalysis data are analyzed, and the results are confirmed with idealized experiments. The leading wind-forced seasonal cycle is excluded to focus on the effect of the eddy. The warm eddy southwest of Taiwan is shown to generate a northward flow, whereas the cold eddy produces a southward current. The effect of the eddy penetrates onto the shelf through the joint effect of baroclinicity and relief (JEBAR). The cross-isobath fluxes lead to shelfward convergence and divergence, setting up the modulation of the sea level slope. The resulting along-strait current anomaly eventually affects a wide area of the Taiwan Strait. The stronger eddy leads to larger modification of the cross-shelf flows and sea level slope, producing a greater transport anomaly. The composite Sea-Viewing Wide Field-of-View Sensor chlorophyll-a (Chl-a) serves as an indicator to show the change in Chl-a concentration in the strait in response to the eddy-induced current. During the warm eddy period, the current carries the southern water of lower concentration northward, reducing Chl-a concentration in the strait. In contrast, Chl-a is enhanced because the cold eddy–induced southward current carries the northern water of higher concentration southward into the strait.

1. Introduction

The Taiwan Strait lies between southeastern China and Taiwan (Fig. 1) and is oriented in southwest and northeast directions. The water depths in the Taiwan Strait are generally shallower than 50 m, except for the deeper Penghu Channel to the southwest of Taiwan. With a length of ~350 km, the Taiwan Strait is a passage connecting two large marginal seas: the South China Sea to the south and the East China Sea to the north. Although the strait is shallow, it plays an essential role in the water exchange between the two marginal seas and the Pacific Ocean (Wyrtki 1961; Liu et al. 2000).

The volume transport of the Taiwan Strait had been investigated since the early 1960s. Based on sea level station data, Wyrtki (1961) estimated the Taiwan Strait transport to be less than 1 Sverdrup (Sv; 1 Sv $\equiv 10^6\,m^3\,s^{-1}$) in July and December. Fang et al. (1991) combined several in situ current meter datasets to obtain transport values of 3.1 Sv in summer and 1.0 Sv in winter and an annual-mean transport of 2 Sv. Using the observed shipboard acoustic Doppler current profiler (sb-ADCP), Wang et al. (2003) calculated a mean transport of 1.8 Sv, which was stronger in July (2.7 Sv) and weaker in January (0.9 Sv). Jan et al. (2006) used cluster analysis for the ADCP data from 1999 to 2001 to derive a transport of 1.16–2.34 Sv from March to August that changes into a weak transport of −0.1 Sv southward in winter. Negative transport was also observed by Lin et al. (2005) using a bottom-mounted ADCP during October–December 1999 under a strong northeasterly monsoon. The modeling study by Wu and Hsin (2005) proposed a transport of 1.09 ± 1.67 Sv based on a 5-yr run. Their simulation also shows stronger transport in summer than that in winter.

Corresponding author address: Yu-Lin Chang, S609, Lecture and Research Building 88, Sec. 4, Tingzhou Rd., Taipei 10677, Taiwan.
E-mail: ychang@ntnu.edu.tw

DOI: 10.1175/JPO-D-14-0248.1

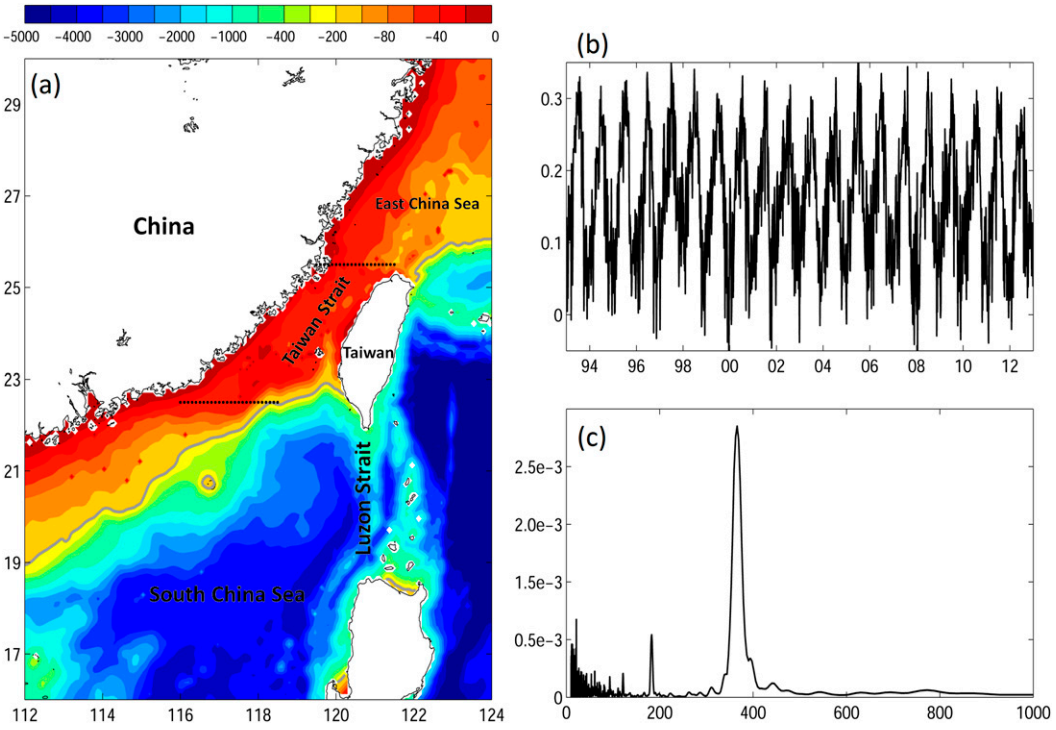

FIG. 1. (a) Bathymetry (m) of the study region and (b) the time series of mean along-strait velocity ($m\,s^{-1}$) taken from the area between the two black dotted lines in (a). (c) Power spectra (x axis represents days, and y axis is the power in Watts) for the along-strait velocity in (b).

The Taiwan Strait transport reveals strong seasonal signals that are stronger in summer than those in winter. The annual-mean transport in the Taiwan Strait is northward, flowing along the strait. The net northward transport under the absence of wind is induced by the persistence of sea level slope (Yang 2007). The East Asia monsoon is considered to be the main forcing responsible for the seasonal variation (Wang et al. 2003; Wu and Hsin 2005; Jan et al. 2006; Wu et al. 2007). The summer southwesterly wind together with the persistent sea level slope causes a negative pressure gradient that drives the stronger along-strait flow. In winter, the northeasterly wind competes with the background pressure gradient, resulting in weaker northward or even southward flow (Oey et al. 2014). On the basis of empirical orthogonal function (EOF) results, a recent study by Oey et al. (2014) offered a different mechanism of the wind-driven, fluctuating pressure gradient on a time scale of days. They determined that the northeasterly wind sets up the high sea level to the southwestern strait such that the flow moves northward while the wind relaxes. Moreover, W.-Z. Zhang et al. (2014) used a 4-yr numerical simulation and suggested that the effect of typhoons can reduce the Taiwan Strait transport by up to 0.45 Sv and the annual mean by 0.09 Sv. The wind is considered to be the force affecting the Taiwan Strait Current variation for time scales of days to seasons.

In the present study, a new candidate other than wind is proposed. Oceanic eddies originate almost everywhere in the world's oceans. Mesoscale eddies play important roles in transporting heat and in biochemical processes (Volkov et al. 2008; Chelton et al. 2011; Mahadevan et al. 2012). The mass transport by global mesoscale eddies of 30–40 Sv has a magnitude comparable to that of large-scale, wind-driven, and thermohaline circulation (Z. Zhang et al. 2014). Eddies are characterized by their distinct sea surface height from the ambient water. The effect of warm-core eddies on the along-shelf pressure gradient in the Middle Atlantic Bight was demonstrated by Xu and Oey (2011), who showed that the impingement of warm-core eddies upon the shelf break can produce sea level changes on the shelf. Mesoscale eddy activities are often observed in southwestern Taiwan (Nan et al. 2011). The mesoscale features to the southwest of Taiwan are attributed to locally formed eddies, westward penetration subtropical countercurrent eddies, Kuroshio-shedding eddies, or the Kuroshio intrusion through the Luzon Strait (Li et al. 1998; Nan et al. 2011; Sheu et al. 2010). The present

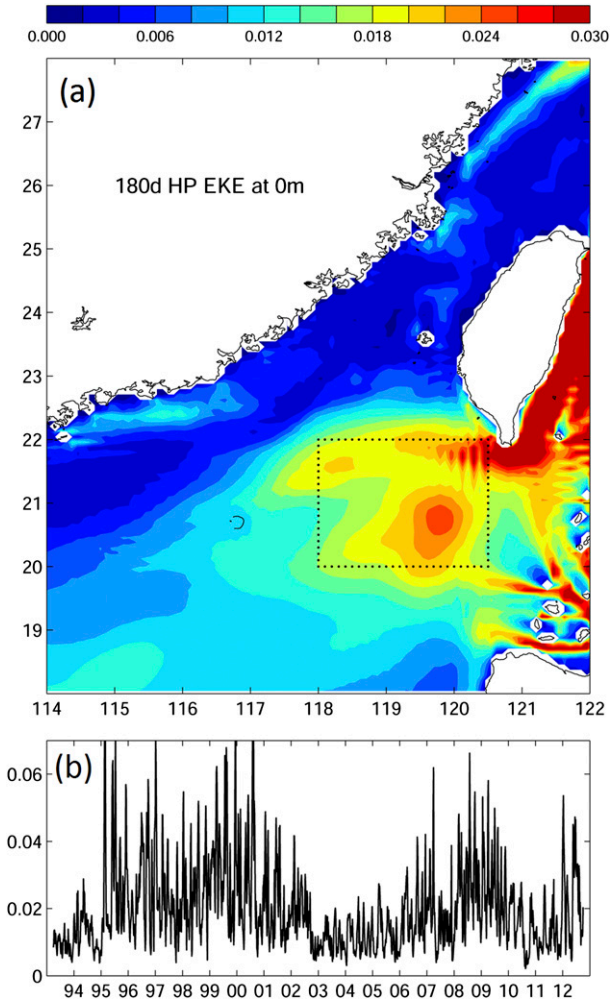

FIG. 2. (a) 20-yr mean EKE ($m^2 s^{-2}$) with 180-day high pass and (b) time series of the EKE of the black box in (a).

study aims to demonstrate that eddies can create external forcing to affect the variation of the Taiwan Strait Current, even though they cannot intrude into the shallow coastal water owing to their deeper vertical structures.

2. Data and methods

The analysis in this study is based on the 20-yr (1993–2012) model reanalysis results from Japan Coastal Ocean Predictability Experiment 2 (JCOPE2; Miyazawa et al. 2009). JCOPE2 is a data-assimilating ocean model based on the Princeton Ocean Model (POM) and includes a generalized coordinate system (Mellor et al. 2002). The domain encompasses the western North Pacific Ocean (10.5°–62°N, 108°–180°E) with a horizontal resolution of 1/12° and 46 vertical layers. The lateral boundary conditions are determined from a basinwide model using a one-way nesting method (Guo et al. 2003). The model is forced by wind stresses, heat, and salt fluxes from the 6-hourly National Centers for Environmental Prediction–National Center for Atmospheric Research (NCEP–NCAR) reanalysis data. In situ temperature and salinity data from the Advanced Very High Resolution Radiometer/multichannel sea surface temperature (AVHRR/MCSST), U.S. Global Ocean Data Assimilation Experiment (USGODAE) project (http://www.usgodae.org/), Colorado Center for Astrodynamics Research (CCAR) near-real-time altimetry data (http://eddy.colorado.edu/ccar/data_viewer/index), and Global Temperature and Salinity Profile Programme (GTSPP) are assimilated into the model. Details of the model setup and descriptions have been reported by Miyazawa et al. (2009).

Idealized experiments were conducted to isolate the effect of eddies. The model is based on the message passing interface (MPI) version of POM (Blumberg and Mellor 1987; Jordi and Wang 2012; Oey et al. 2013). The domain covers the North Pacific Ocean from 16°S to 70°N and from 98°E to 73°W at 0.1° × 0.1° horizontal resolution with 41 sigma levels. All surface fluxes are zero. Climatology *World Ocean Atlas* (*WOA*) data from the National Oceanographic Data Center (NODC; http://www.nodc.noaa.gov/OC5/WOA05/pr_woa05.html) for temperature T and salinity S were first used to diagnostically integrate the model to steady state, which yielded current fields in balance with the corresponding densities. Starting from the balanced state, the NCEP–NCAR wind climatology is constantly applied to maintain the Kuroshio. The wind is turned off west of 130°E to eliminate the local wind effect. The basic run is continued from the balanced state. For the eddy cases, we inject a warm/cold eddy with a radius of 150 km, centered at 21°N, 119°E. The eddy injection method follows that reported by Shaw (1994) and Xu and Oey (2011). The warm/cold eddy is gradually ramped up over a period of 10 days. To conserve heat, the same heat is removed by specifying a uniform upward/downward surface heat flux over the model domain.

3. Results

a. Signals other than seasonal

In this study, the x and y directions are rotated 30° clockwise from true north; positive y points along-strait northeastward. Figure 1b plots the time series of the Taiwan Strait mean along-strait current. The sampling area is enclosed by the two dotted lines in Taiwan Strait (Fig. 1a). The along-strait current reveals strong seasonal variation as well as higher-frequency signals

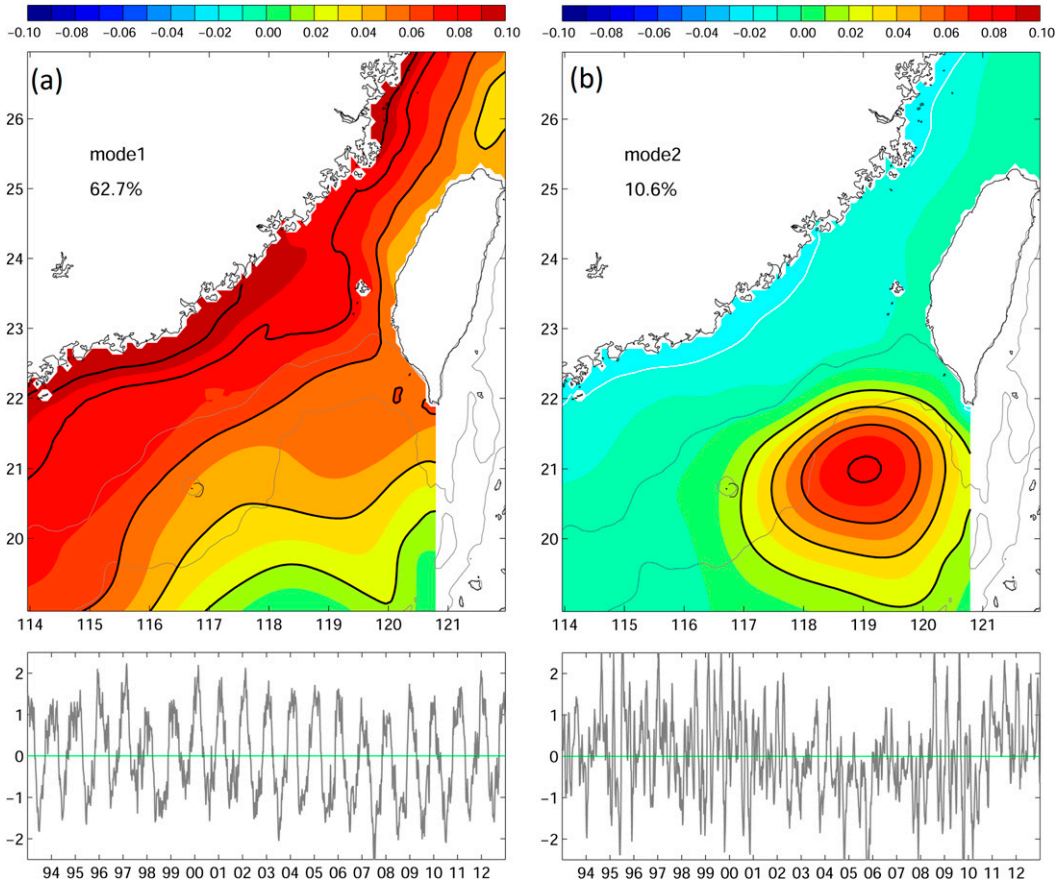

FIG. 3. EOF of sea surface elevation (m) for (a) mode 1 and (b) mode 2. (top) Eigenvectors and (bottom) PCs. Gray contours in the top panels indicate 200- and 2000-m isobaths.

(Fig. 1b). The seasonal cycle is shown as the largest peak in the power spectra analysis. The secondary peaks capture the intraseasonal signals with periods shorter than 180 days (Fig. 1c). W.-Z. Zhang et al. (2014) suggested that the short-time fluctuation is induced by intense weather events such as storms and winter wind bursts. In addition to wind, the effects of eddies are considered in the present study. The 20-yr mean eddy kinetic energy [EKE; $(u'^2 + v'^2)/2$] is plotted in Fig. 2. Slower varying signals are excluded by applying a 180-day high-pass filter. The large EKE appears to the southwest of Taiwan (Fig. 2a). This active eddy activity southwest of Taiwan was also reported by Nan et al. (2011), who used 17-yr satellite altimetry data. The high EKE region, from 20° to 22°N and from 118° to 120.5°E, is chosen to represent the eddy activity following Nan et al. (2011). The time series of domain-averaged EKE is plotted in Fig. 2b. The decadal signal shift at approximately 2002 may be related to Pacific decadal oscillation (PDO) (Soeyanto et al. 2014). Time-scale variation longer than seasonal is not considered in this study. The link between eddy activity and the Taiwan Strait flow is next demonstrated through EOF and singular value decomposition (SVD) analyses.

b. *EOF and SVD analyses*

The 3.5-month (1 February–15 May 2012) EOF results reported by Oey et al. (2014) obtained the first mode as the monsoon wind–driven, geostrophic mode. The second mode was the shorter time-scale, wind-forced, fluctuating pressure gradient mode. We extended the concepts of Oey et al. (2014) by using EOF analysis (Kutzbach 1967) with a larger spatial domain and longer time scale. The EOF domain is set from 19° to 27°N and from 114° to 122°E to include the area of high EKE southwest of Taiwan. The time series is every 5 days for 20 yr, covering 1993–2012. The steric height computed from temperature and salinity (Marshall and Plumb 2007) is removed. The high energy Kuroshio is masked out for focusing on the Taiwan Strait Current and eddies. Note that both EOF and SVD analyses are conducted on the basis of the anomaly with the 20-yr mean removed. The leading

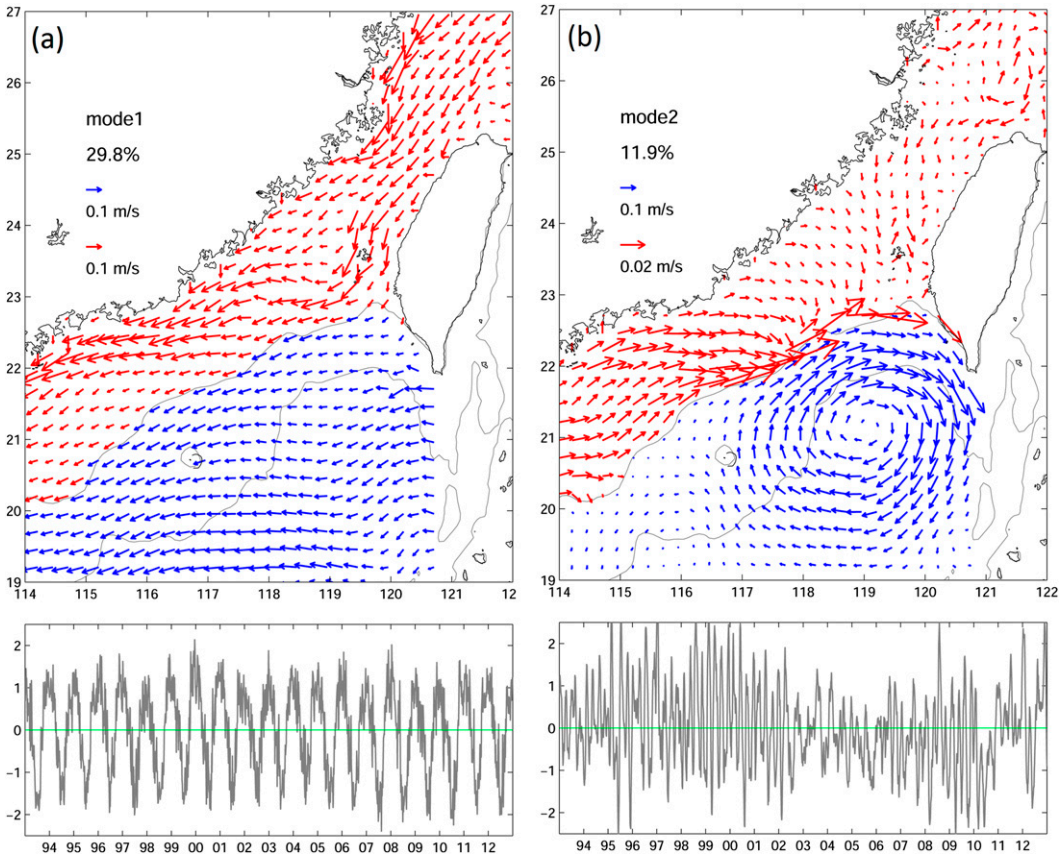

FIG. 4. EOF of surface currents (m s^{-1}) for (a) mode 1 and (b) mode 2. (top) Eigenvectors and (bottom) PCs. Two scales are used for shelf (red) and off-shelf (blue) regions.

modes of EOF on the sea surface height anomaly (SSHA) and surface current are shown in Figs. 3 and 4, respectively. The first mode of SSHA and surface current are both dominated by the seasonal signal (Figs. 3a and 4a, respectively). The first mode of SSHA accounts for 62.7% of the total variance. The surface current has a lower percentage, explaining 29.8% of the total variance. The surface current is nearly geostrophic (Figs. 3a, 4a). This geostrophic relation explains the along-strait current moving southward in winter and northward in summer (Figs. 3a, 4a). The leading mode is consistent with that reported in earlier studies such that the along-strait current flows southward under the northeasterly winter monsoon; during the southwesterly summer monsoon, the current moves northward. The following leading mode of SSHA and the surface current reveals faster variations in principal components (PCs) than those in seasonal components (Figs. 3b, 4b). The mode-2 SSHA shows that the warm eddy southwest of Taiwan corresponds to the positive cross-strait SSHA gradient (Fig. 3b), which is balanced by the northward flow based on the geostrophic relation. Conversely, the negative cross-strait SSHA gradient corresponding to the southward current is related to the cold eddy during the negative PC. The mode-2 surface current also captures an eddy southwest of Taiwan together with the along-strait current in the southern strait (Fig. 4b). The currents to the north are weaker than those to the south and are not geostrophic. The geostrophic and seasonal variations, shown in the first mode of SSHA and the surface current, agree with the first EOF mode reported by Oey et al. (2014). The wind-forced fluctuated pressure gradient mode reported by Oey et al. (2014) does not appear in the leading modes in our analysis, which may be attributed to the different time scales between the two analyses. The EOF analysis suggests a link between mesoscale eddies and the along-strait current; SVD analysis will next show the coupling between the two.

The analysis shown above indicates that the eddy signal has faster fluctuation than seasonal. To focus on the effect of eddies, the seasonal cycle is removed in the following analysis. The SVD analysis (Bretherton et al.

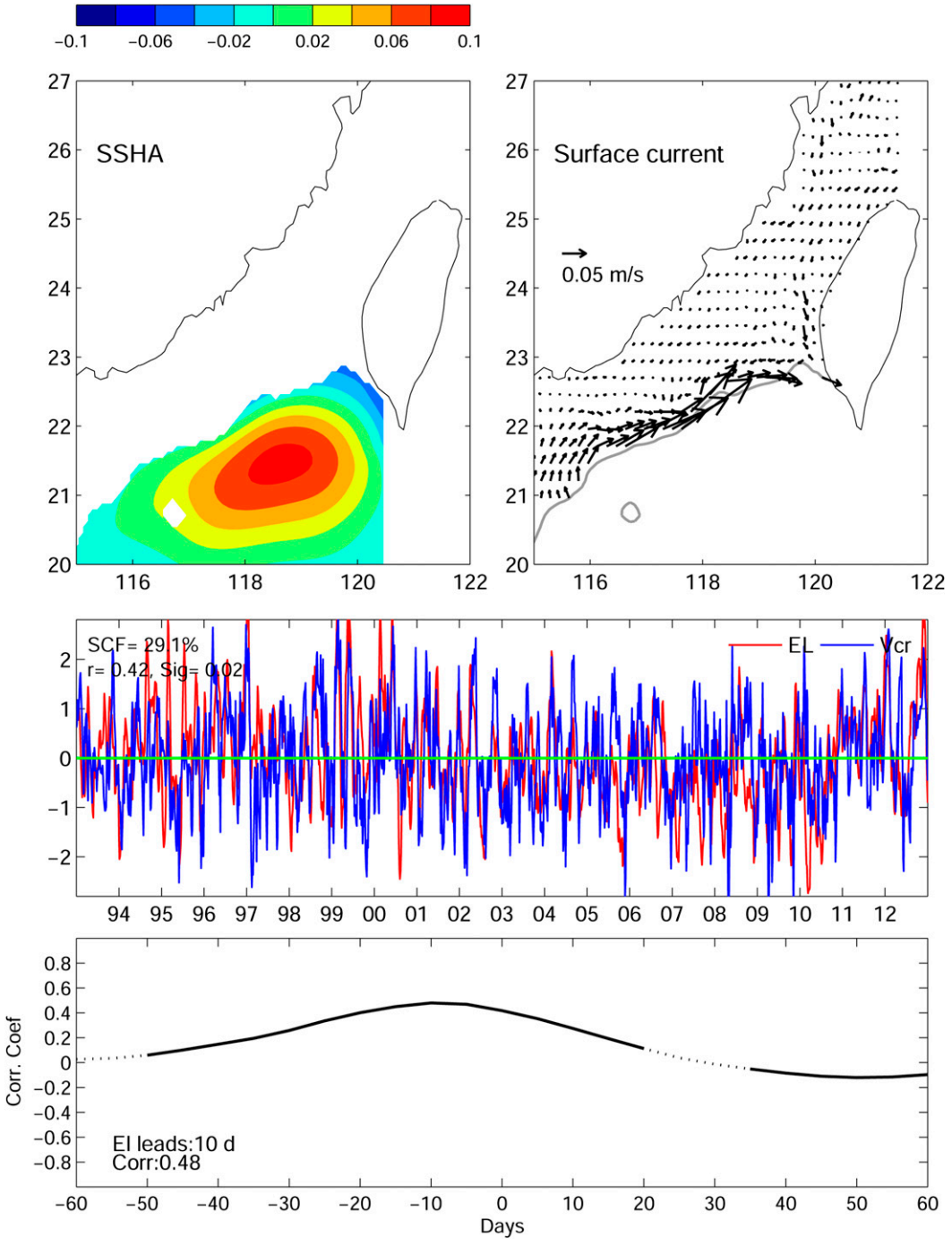

FIG. 5. (top) Mode-1 SVD for the (left) SSHA (m) and the (right) surface current ($m\,s^{-1}$). (middle) Expansion coefficients for the SSHA (red) and surface current (blue). (bottom) The lag correlations between the two expansion coefficients. The value exceeding the 95% significant level is plotted in solid black.

1992) applied on two variables seeks to identify the pair of coupled spatial patterns, with each pair explaining a fraction of the covariance between the two fields. One of the advantages in SVD analysis is that the two variables do not require the same spatial grid, although they must have the same time length. The currents inside the eddy are stronger than the shelf currents induced by the eddy. If the same area is used for both SSHA and shelf current, the coupling is captured within the eddy itself (i.e., eddy's elevation and its current field) rather than being a

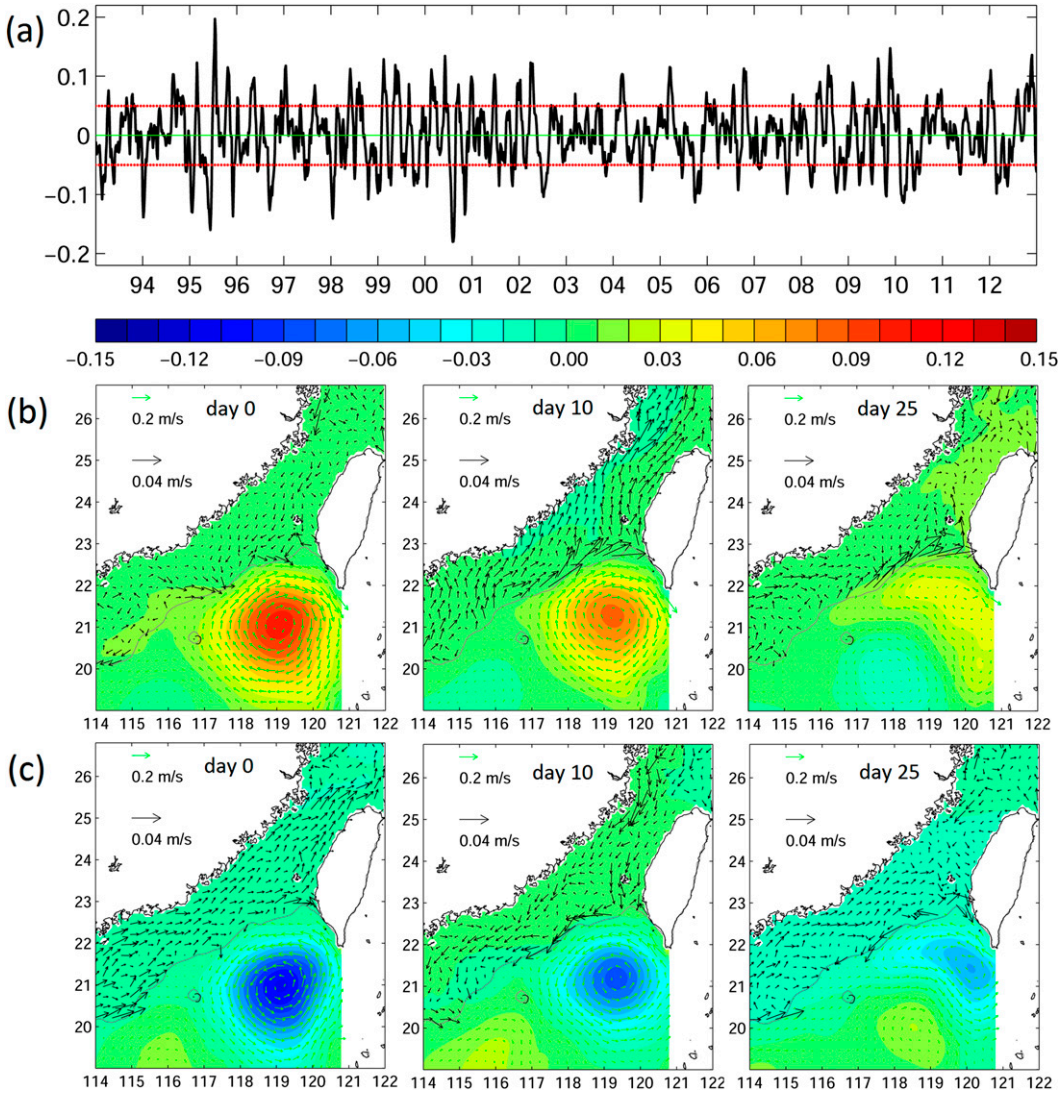

FIG. 6. (a) SSHA (m) taken from the black box in Fig. 2a. Composite (b) warm and (c) cold eddy events on (left) day zero, (middle) day 10, and (right) day 25 are shown. Colors represent the composite SSHA (m), and vectors represent the composite surface current anomaly ($m\,s^{-1}$). Shelf currents follow the black unit scale, and off-shelf flows are represented by the green unit scale.

target of the shelf current. To address the coupling between the eddy and the shelf current, different domains for the two variables are required. The domain of SSHA is chosen off the shelf, south of 23°N, where eddies are observed. The area for the current is set on the shelf, north of 21°N, covering the Taiwan Strait. The first mode of SVD accounts for 29.1% of the total variance, as shown in Fig. 5. The SVD spatial patterns are similar to mode 2 of the EOF (Fig. 4), showing a strong, warm eddy southwest of Taiwan coupled with the northward current south of 23°N. The current inside the Taiwan Strait is weak and southward. The maximum coupling coefficient is 0.48, with SSHA leading the shelf current by 10 days. The EOF and SVD analyses reveal that the monsoon serves as a primary forcing to drive the seasonal shelf flow. The secondary effect by the mesoscale eddies to the southwest of Taiwan is responsible for the shorter time-scale fluctuation. SSHA EOF results show that while a warm eddy appears to the southwest of Taiwan, a positive cross-strait SSHA gradient is observed; the negative cross-strait SSHA gradient appears during the existence of the cold eddy to the southwest of Taiwan. Similar results are detected in the surface current in EOF and SVD analysis. However, the warm eddy coupling with the northward current exists only in the southern strait; the current inside the strait is nearly

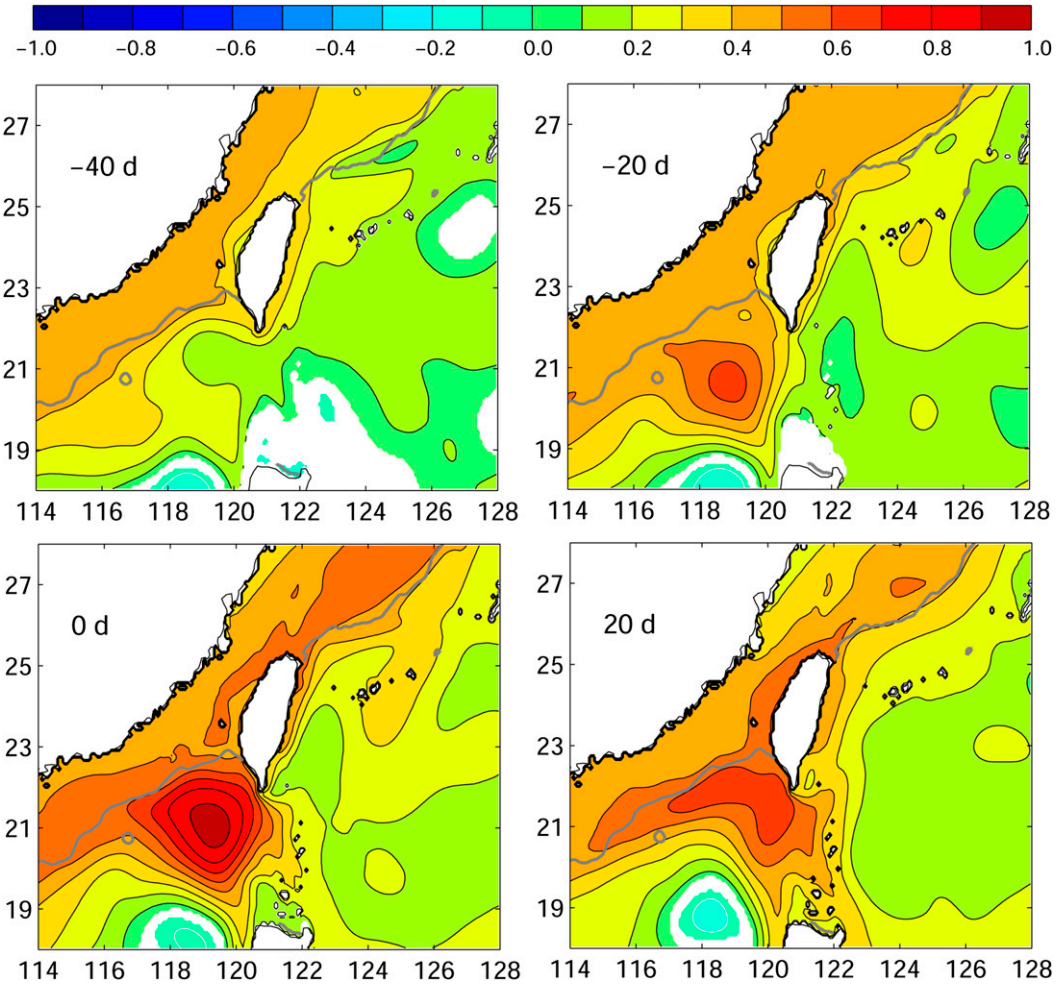

FIG. 7. Lag correlation coefficient between eddy index, which is the domain-averaged SSHA of that shown in the black box in Fig. 2a and SSHA. Values lower than 95% significant levels are in white. Minus *n* day indicates eddy index lags of SSHA by *n* days.

quiet. The response in the strait with a 10-day time lag is illustrated using composite analysis.

c. *Composite events*

The composite method is used to show the manner in which the along-strait current varies with the eddy in sequence. The eddy index is first defined by taking the domain-averaged SSHA (black box in Fig. 2, high EKE region) with the seasonal cycle and interannual signal removed. The eddy index (Fig. 6a) shows high-frequency fluctuation. The period of 90–100 days is determined through power spectra analysis. The maximum eddy strength exceeding the criterion of ±0.05 (m) is chosen for the composite. We have detected 47 warm eddy events and 44 cold eddy events exceeding the threshold. Warm and cold eddy events are sorted into two groups for the composite. The composite day zero is defined as the time at which the eddy index reaches maximum. Figures 6b and 6c show the composite SSHA and the surface current anomaly, respectively. A warm eddy is shown to the southwest of Taiwan on day zero (Fig. 6b, left panel). The along-strait current is southward in the northern strait, and the current west of the eddy moves northward. Then, 10 days later, the along-strait current turns northward in the entire strait (Fig. 6b, middle panel). The warm eddy becomes much weaker and dissipates on day 25, and a cold eddy appears to the south of the warm eddy. The along-strait current remains northward near the shelf break, and the current inside the strait becomes weaker (Fig. 6b, right panel). The case of the cold eddy is similar to the warm eddy event, although the sign is reversed. The along-strait current is northward on day zero, whereas the cold eddy appears southwest of Taiwan (Fig. 6c, left panel). On day 10, the eddy moves slightly northward, and the along-strait current flows southward (Fig. 6c, middle

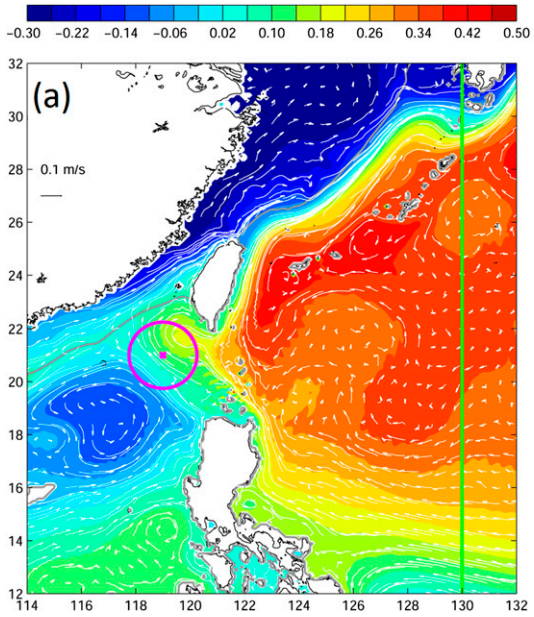

(b)

WOA Climatology T/S
(Diagnostic)

⇩

NCEP/NCAR 20-yr mean wind
(east of 130E)

Case		*Name for Experiment*	*Mean eddy SSHA (m)*
Basic		Exp_0	0.0
Warm eddy	Standard	Exp_w1	0.13
	Strong	Exp_w2	0.17
Cold eddy	Standard	Exp_c1	-0.15
	Strong	Exp_c2	-0.20

FIG. 8. (a) Diagnostic SSHA (m, color) and surface current (m s^{-1}, white vector) from the idealized experiments. The pink circle indicates the location of the injected eddy. The green line marks 130°E for the border of wind switch. (b) Flowchart and list of experiments.

panel). The cold eddy weakens on day 25, and a warm eddy is observed to the south. The current weakens and even changes direction in the southern strait (Fig. 6c, right panel). The criteria of 0 (m) and 0.1 (m) are repeated for the composite, and the conclusion remains the same.

To determine the source of the eddies, spatial lag correlation is conducted between the eddy index (Fig. 6a) and the SSHA (Fig. 7). In this study, the seasonal cycle is removed to focus on the intraseasonal time scale. The lag correlation shows that the correlation increases locally. The eddies in the intraseasonal time scale are locally formed rather than propagating from the Pacific Ocean.

d. Mechanisms

To examine the mechanism of the eddies' effect on the Taiwan Strait Current, idealized experiments are conducted. The model details are given in section 2. The experiment list and flowchart are summarized in Fig. 8. Figure 8a plots the diagnostic sea surface height and surface current obtained from climatology. A preexisting warm eddy appears southwest of Taiwan. To distinguish the effect of the injected warm/cold eddy to the Taiwan Strait, the basic experiment (Exp_0; Fig. 8b) is subtracted from the eddy experiments (i.e., $\mathrm{SSHA}_{\mathrm{Exp\_w1}} = \mathrm{SSH}_{\mathrm{Exp\_w1}} - \mathrm{SSH}_{\mathrm{Exp\_0}}$).

Figure 9a shows the Taiwan Strait transport anomaly (with Exp_0 subtracted) for the eddy experiments. The transport is integrated from the sea surface to the bottom across 24.2°N near the center of the strait. The transport begins to change around days 15–20. The change in transport lasts until the injected eddy dissipates (approximately 40 days). The transport strengthens in the case of the warm eddy. Conversely, the transport weakens under the cold eddy conditions. A stronger eddy is related to greater changes in transport.

We then examine the cause of the transport change with the existence of eddies. As reported by Oey et al. (2014, their appendix) for the case of the Taiwan Strait Current, the linearized, depth-integrated [from bottom $z = -h(x)$ to surface $z = 0$] dynamical equations for a homogeneous fluid are as follows:

$$-fv_a h = -gh\frac{\partial \eta}{\partial x} + \tau_o^x - \tau_b^x, \tag{1}$$

$$fu_a h = -gh\frac{\partial \eta}{\partial y} + \tau_o^y - \tau_b^y, \quad \text{and} \tag{2}$$

$$\frac{\partial (u_a h)}{\partial x} + \frac{\partial (v_a h)}{\partial y} = 0, \tag{3}$$

where x and y are in the cross-strait and along-strait directions, respectively; h is the water depth; η is the surface elevation; $\mathbf{u}_a = (u_a, v_a)$ is the depth-averaged velocity; f is the Coriolis parameter; $\boldsymbol{\tau}_o = (\tau_o^x, \tau_o^y)$ is the kinematic wind stress vector; and $\boldsymbol{\tau}_b = (\tau_b^x, \tau_b^y)$ is the kinematic bottom stress vector, which is parameterized as

$$\boldsymbol{\tau}_b = r\mathbf{u}_a, \tag{4}$$

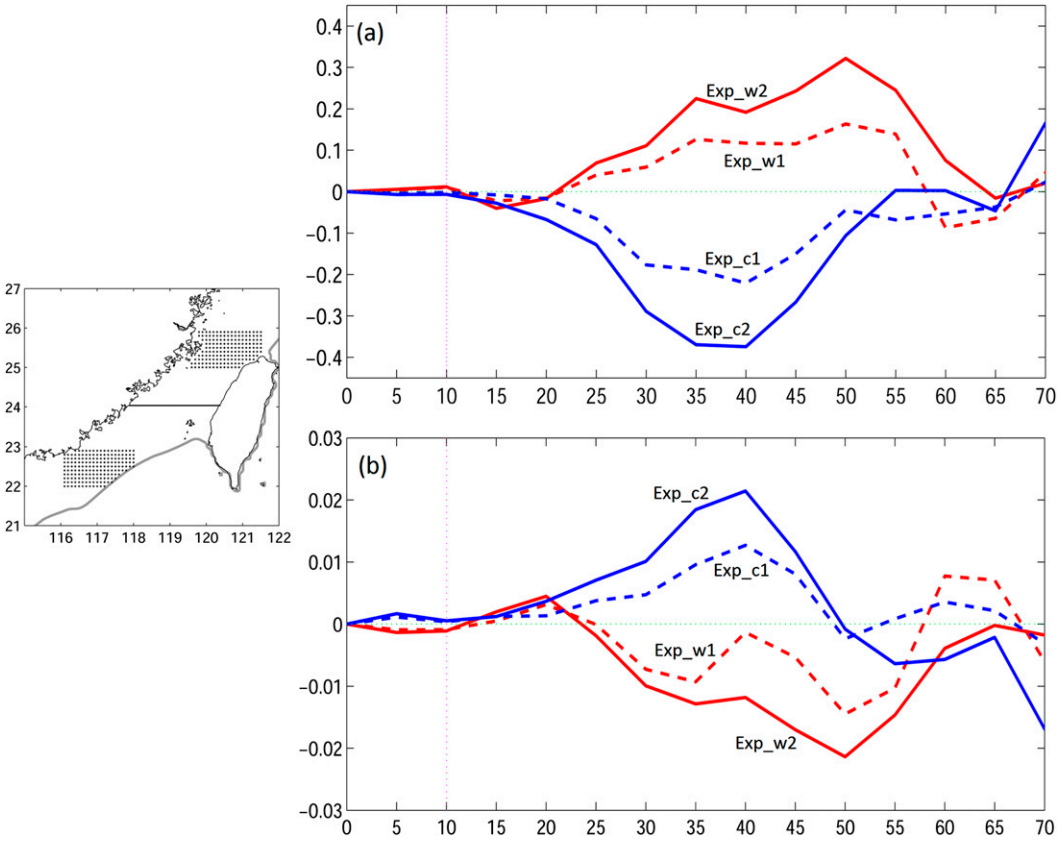

FIG. 9. Time series of (a) transport anomaly (Sv) and (b) sea level slope anomaly (m) from the idealized experiments. The x axis represents days. The inset shows the locations from which the transports were taken (24.2°N; black line) and sea level slope using north (dots north of 25°N) minus south (dots south of 23°N).

where r is a constant friction coefficient. In the Taiwan Strait, the cross-strait bottom friction and wind stress are negligible in comparison to along-strait components. Equations (1) and (2) then respectively become

$$-fv_a h = -gh\frac{\partial \eta}{\partial x}, \quad \text{and} \tag{5}$$

$$fu + rv_a = -gh\frac{\partial \eta}{\partial y} + \tau_o^y. \tag{6}$$

The cross-strait momentum is the geostrophic balance. In the idealized experiment, the wind stress is dropped according to the model setting, and the cross-strait velocity is weak. The along-strait momentum is approximately

$$rv_a \approx -gh\frac{\partial \eta}{\partial y}. \tag{7}$$

Next, the contributions from eddies and the large-scale pressure gradient are separated, and Eq. (7) is rewritten as

$$r(v_{a\_\mathrm{pg}} + v_{a\_\mathrm{eddy}}) \approx -gh\left(\frac{\partial \eta}{\partial y}_{\mathrm{pg}} + \frac{\partial \eta}{\partial y}_{\mathrm{eddy}}\right). \tag{8}$$

By subtracting Exp_0, the anomaly in the eddy case is

$$rv_{a\_\mathrm{eddy}} \approx -gh\frac{\partial \eta}{\partial y}_{\mathrm{eddy}}. \tag{9}$$

In Eq. (9), the along-strait current is proportional to the minus sign of the along-strait sea level slope. The northward flow corresponds to a negative sea level slope, and the southward current is associated with a positive sea level slope. The along-strait sea level slopes from the eddy experiments are computed. Following Wu and Hsin (2005), the sea level slope takes the mean sea level at the northern strait (25°–26°N; inset in Fig. 9) minus the mean sea level at the southern strait (22°–23°N). The results show that the warm eddy induces a negative sea level slope, leading to the northward flow [red curves in Fig. 9; Eq. (9)]. On the contrary, the positive sea level slope is balanced by the southward current in the case of the cold eddy [blue curves in Fig. 9; Eq. (9)]. A stronger (positive/negative) eddy corresponds to a larger sea level tilt, resulting in a stronger along-strait flow [Fig. 9; Eq. (9)].

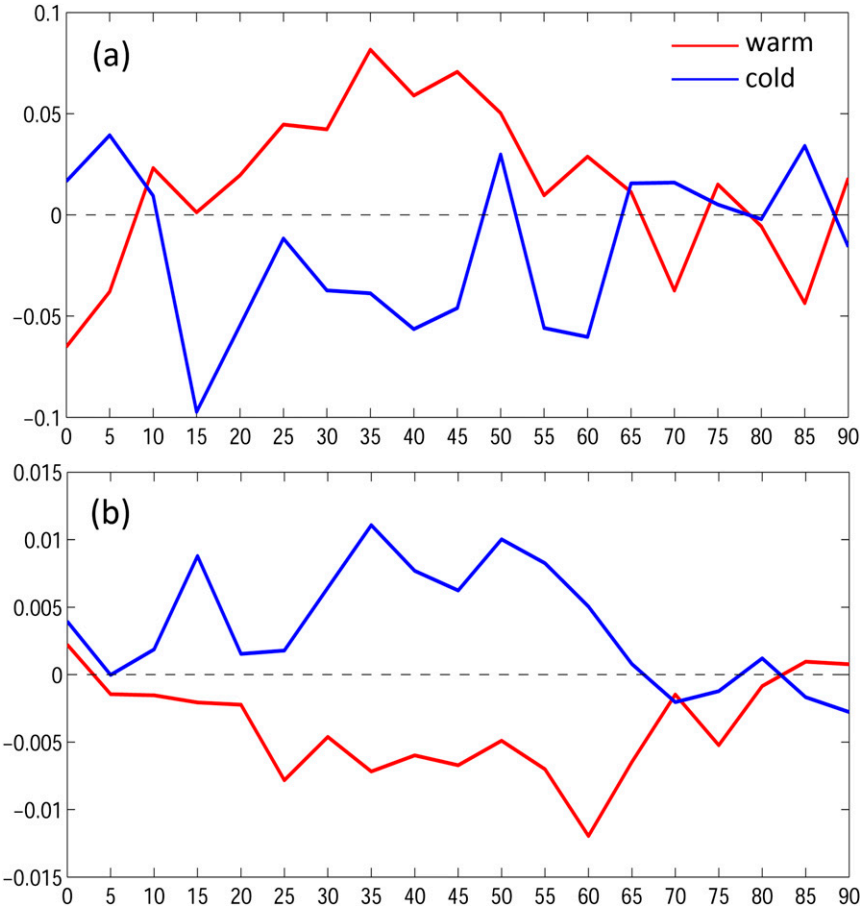

FIG. 10. As in Fig. 9, but for JCOPE2.

The transport anomaly and sea level slope for JCOPE2 are repeated following the same composite as that shown in Fig. 6; results similar to those of the idealized experiments are shown in Fig. 10. When the warm eddy approaches the strait, the sea level slope becomes negative (higher sea level to the southern strait) and the transport shifts northward (red curves in Fig. 10). This process can last for 40–50 days until the eddy weakens. The case of the cold eddy results in the opposite sign, which makes the sea level slope positive and the along-strait current flow southward (blue curves in Fig. 10). Note that with the existence of wind stress in JCOPE2, the balance follows Eq. (6); the transport and sea level slope are nearly out of phase. Because of the modification from the wind stress, the variation in transport does not closely follow the change in sea level slope shown in the idealized experiment.

The vorticity equation is next analyzed to determine the mechanism wherein the eddy effects are transferred onto the shelf to produce a sea level slope. Following Xu and Oey (2011) and Oey et al. (2014), the depth-averaged vorticity equation derived from the depth-averaged momentum equations is

$$\frac{\partial \zeta}{\partial t} + \mathbf{U}\cdot\nabla\left(\frac{f+\zeta}{D}\right) - \frac{\partial \eta}{\partial t}\left(\frac{f+\zeta}{D}\right) = k\cdot\left[\nabla(\chi)\times\nabla\left(\frac{1}{D}\right)\right] + \nabla\times\left(\frac{\tau_o-\tau_b}{D}\right), \tag{10}$$

where ζ is the curl of the depth-averaged velocity $\mathbf{u}_a$; $D = h + \eta$ is the total water depth; $\mathbf{U} = D\mathbf{u}_a$ is the transport vector per unit length; k is the z-unit vector; $\chi = \int_{-h}^{0} zb\,dz$; and $b = g(\rho/\rho_o)$ is the buoyancy. By approximating $D \approx h$, the time-dependent terms for the composite are negligible, and Eq. (10) becomes

$$\mathbf{U}\cdot\nabla\left(\frac{f}{h}\right) \approx -\mathbf{U}\cdot\nabla\left(\frac{\zeta}{h}\right) + k\cdot\left[\nabla(\chi)\times\nabla\left(\frac{1}{h}\right)\right] + \nabla\times\left(\frac{\tau_o}{h}\right) - \nabla\times\left(\frac{\tau_b}{h}\right). \tag{11}$$

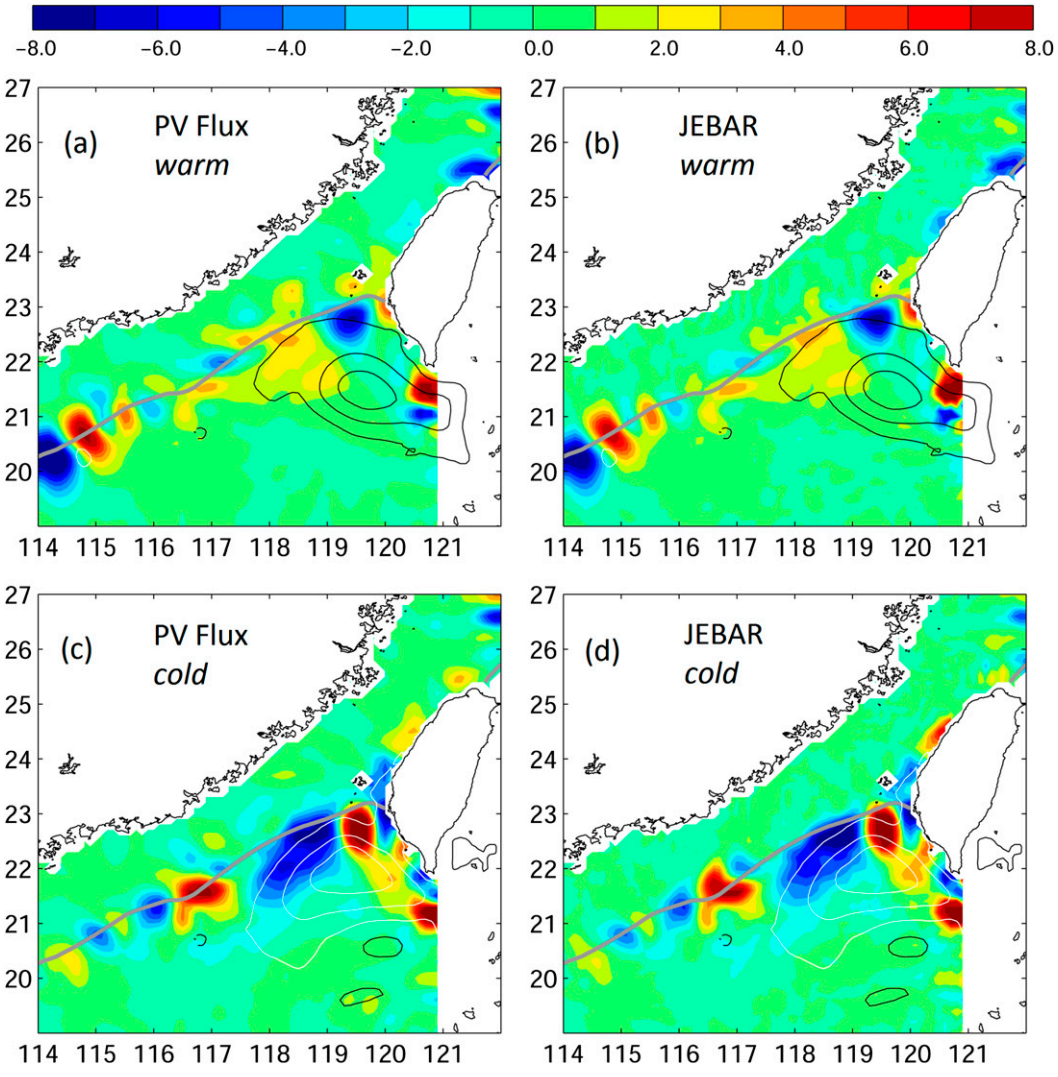

FIG. 11. Composite (a),(c) PV flux and (b),(d) JEBAR for cases of (top) warm eddy and (bottom) cold eddy. Units are $10^{-11}\,s^{-2}$. The superimposed black and white contours represent composite SSHAs (m). The contour interval is 0.05 m. The gray curve represents the 200-m isobath.

The left-hand side of Eq. (11) is the potential vorticity (PV) flux, which represents the horizontal advection of the geostrophic PV. The first term on the right-hand side is the advection of relative vorticity. The second term is the joint effect of baroclinicity and relief (JEBAR) term (Mertz and Wright 1992). The third term is the curl of depth-distributed wind stress, and the last term is the negative curl of depth-distributed bottom stress. All the terms are computed in the idealized experiments to determine which ageostrophic term on the right-hand side of the equation dominates the cross-isobath PV flux. The 30-day periods with large sea level slope changes are selected for the composite (Fig. 9). Days 27–57 are chosen for the warm eddy case, and days 20–50 are selected for the cold eddy experiment. The standard cases (Exp_w1 and Exp_c1) are demonstrated because the eddy SSHA in these cases is similar to that in JCOPE2.

Figure 11 plots the composite dominate terms, PV flux, and the JEBAR term together with the composite SSHA. Since all other terms are approximately one order of magnitude smaller, the figures are not shown. In the case of the warm eddy, the water is more buoyant toward its center. In the southern half of the eddy, $\nabla(\chi)$ points northeastward, and $\nabla(1/h)$ points onshore toward the coast. The resulting JEBAR is positive (Fig. 11b), which is balanced by the positive PV flux (Fig. 11a), corresponding to the onshore flow. Similarly, in the northern half of the eddy, $\nabla(\chi)$ changes direction to point southwestward, and the resulting JEBAR

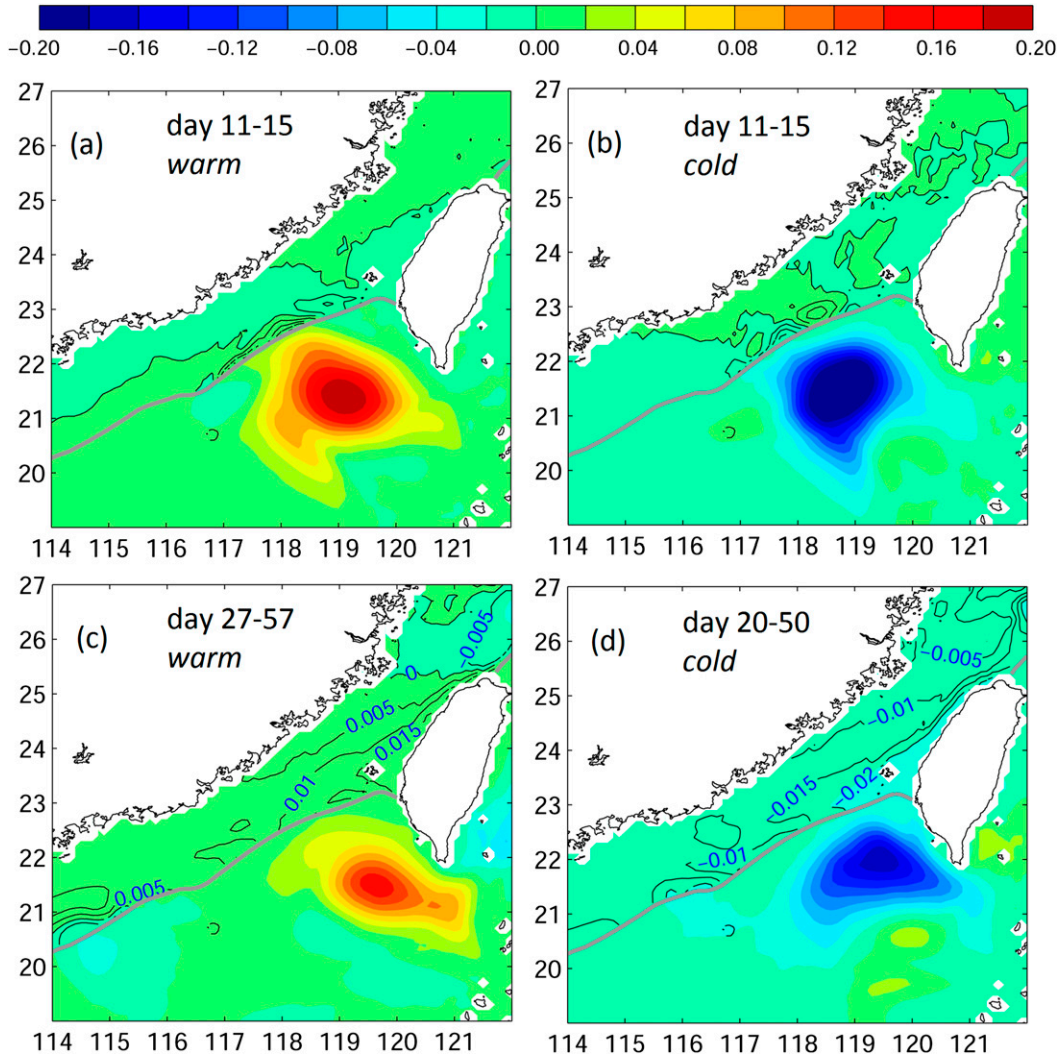

FIG. 12. Composite SSHA (m) for (a),(b) days 11–15 and (c),(d) 30-day composite for cases of (left) warm eddy and (right) cold eddy. The contour interval for the black contours on the shelf is 0.005 m. The gray curve represents the 200-m isobath.

becomes negative. The balanced negative PV flux, therefore, leads to the offshore flow. Thereafter, the shelfward convergence and divergence produce a northward sea level tilt (higher to the south). This phenomenon is shown in Fig. 12. On days 11–15, after the injection of the eddy and before the transport begins to change, a sea level anomaly dipole is detected on the shelf, west of the eddy (Fig. 12a). The onshore and offshore movements continue to increase and decrease sea level over time. The water then spreads out, and the signal ultimately expands into the strait. With the effect of Coriolis force, the sea level contours tilt in southwest and northeast directions (Fig. 12c). The sea level becomes higher in the south and east, leading to the northward transport (Fig. 9a).

We note that the sea level contour is concentrated to the right of the strait, which is similar to the concept of the arrested topography wave proposed by Csanady (1978). Combining Eqs. (3), (5), and (6) by eliminating u and v, the equation for surface elevation is

$$\frac{\partial^2 \eta}{\partial x^2} + \frac{f}{r}\frac{\partial h}{\partial x}\frac{\partial \eta}{\partial y} = 0. \tag{12}$$

Equation (12) is identical to Eq. (3) in Csanady (1978). The eddy imposes the sea level gradient at the shelf break, serving as the boundary condition. The solution therefore has exponential decay away from the eddy, which results in the condensed sea level to the right side of the strait. The same analogy applies in the case of the cold eddy. The

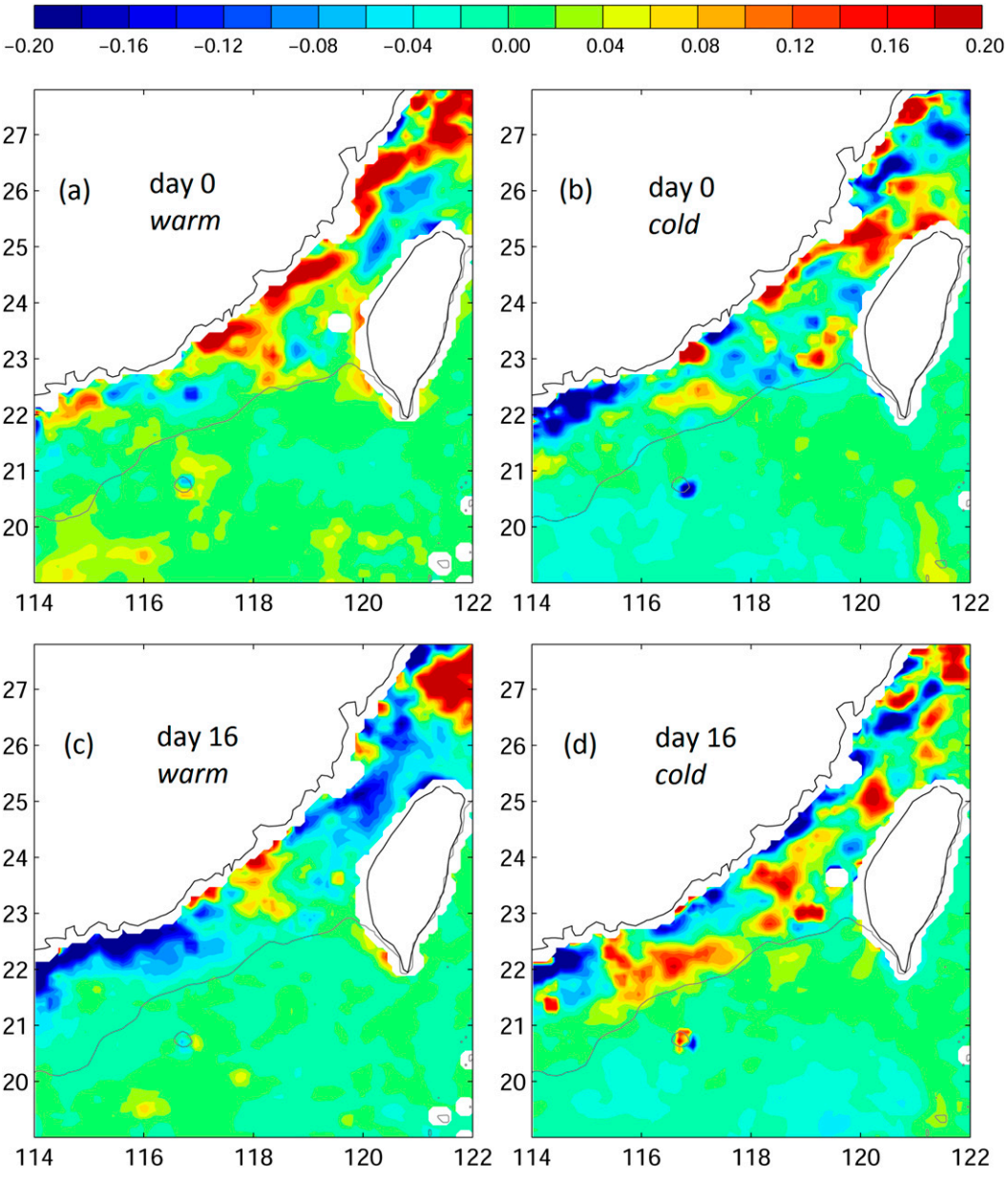

FIG. 13. Composite Sea-Viewing Wide Field-of-View Sensor Chl-a (mg m^{-3}) for (a),(b) day zero and (c),(d) day 16 for cases of (left) warm eddy and (right) cold eddy. The gray curve represents the 200-m isobath.

center of the cold eddy is less buoyant. With the same topography, the JEBAR sign is opposite that in the warm eddy case (Figs. 11c,d). The resulting shelfward divergence and convergence produce a southward sea level tilt that is higher to the north of the eddy (Fig. 12b). Days later, the lower sea level south and east of the strait is balanced by the southward current (Figs. 12d, 9a). The right-side concentration signal is also apparent.

The stronger eddy cases (Exp_w2 and Exp_c2) show similar results with more significant responses (Fig. 9). The larger buoyancy gradient in the stronger eddy results in greater JEBAR. The corresponding stronger cross-shelf flow leads to a higher sea level tilt, which later results in a more enhanced transport anomaly.

Sensitivity experiments are conducted to test the results. The run with a perturbed initial condition leads to the same conclusion. The other experiment applies wind throughout the domain. Since the basic experiment (Exp_0_wind; with wind in this case) is subtracted to show the effect of the eddy, the cases with wind show eddy effects that are highly similar to those in the original sets.

4. Summary and discussion

The present study, based on the 20-yr JCOPE2 reanalysis data, explores the roles of eddies in modifying the Taiwan Strait Current. Apart from the well-documented monsoon-forced seasonal variation, eddy signals with higher-frequency fluctuation are also observed. The effects of the eddy penetrate onto the shelf through the JEBAR effect and eventually spread into a wide area of coastal water. The opposite signs of buoyancy gradients south and north of the eddy result in opposite directions of cross-isobath fluxes, which lead to the shelfward convergence and divergence and set up the modulation of the sea level slope. The warm eddy induces a northward sea level tilt, resulting in a northward, along-strait flow tendency. Conversely, the cold eddy tends to produce a southward sea level slope, leading to a southward transport tendency. The stronger eddy results in a larger modulation of cross-shelf flow and sea level slope, producing a greater transport anomaly.

Eddies contribute to the changes in Taiwan Strait transport. Changes in ocean current can also influence the biochemical environment. Sea-Viewing Wide Field-of-View Sensor chlorophyll-a (Chl-a) data (O'Reilly et al. 1998) are used to show the changes due to eddies. These data were documented as overestimation in the coastal region (Hyde et al. 2007). In the present study, Chl-a is used as an indicator; the absolute value is not addressed. The same composite method (Fig. 6) is applied. The dataset used for the composite has 9-km resolution, every 8 days for 1998–2010; the seasonal cycle is removed. On day zero (Figs. 13a,b), the composite shows negative (positive) anomalies southwest of Taiwan, where the warm (cold) eddy is located. On day 16, Chl-a becomes less than that on day zero in the case of the warm eddy (Fig. 13c). For the cold eddy composite, Chl-a increases in the southern and central regions of the strait (Fig. 13d). The chlorophyll concentration is generally higher in the northern China Seas (i.e., Yellow Sea and East China Sea) than that in the South China Sea (Tang et al. 1998). The chlorophyll content in the Yangtze River estuary is particularly significant. The warm eddy leads to a northward along-strait current, carrying the water of lower concentration from the south to reduce Chl-a concentration in the strait. During the effective period of the cold eddy, the resulting southward current carries the water of higher concentration southward, enhancing Chl-a in the strait.

This research explains the mechanism by which mesoscale eddies affect Taiwan Strait transport in an intraseasonal time scale; the same concept can be used for seasonal or longer time scales. Considering the leading seasonal variation in the Taiwan Strait, additional factors are involved. The seasonal Kuroshio intrusion, winter Chinese coastal water, and monsoon wind may all play roles in modifying the pressure field in the Taiwan Strait. Detailed dynamics for seasonal variation are a topic worthy of future study.

Acknowledgments. We thank the reviewers, whose comments improved the manuscript. Useful discussion with Dr. Tsubasa Kodaira is appreciated. AVHRR/MCSST, USGODAE project, CCAR near-real-time altimetry data, and GTSPP are acknowledged for providing data for model assimilations. YLC is supported by the Ministry of Science and Technology of Taiwan under Grant 102-2611-M-003-003-MY3. XG and YM are supported by JSPS KAKENHI (26287116).

REFERENCES

Blumberg, A. F., and G. L. Mellor, 1987: A description of a three-dimensional coastal ocean circulation model. *Three-Dimensional Coastal Ocean Models, Geophys. Monogr. Coastal Estuarine Sci.,* Vol. 4, Amer. Geophys. Union, 1–16, doi:10.1029/CO004p0001.

Bretherton, C. S., C. Smith, and J. M. Wallace, 1992: An intercomparison of methods for finding coupled patterns in climate data. *J. Climate,* **5,** 541–560, doi:10.1175/1520-0442(1992)005<0541:AIOMFF>2.0.CO;2.

Chelton, D. B., M. G. Schlax, and R. M. Samelson, 2011: Global observations of nonlinear mesoscale eddies. *Prog. Oceanogr.,* **91,** 167–216, doi:10.1016/j.pocean.2011.01.002.

Csanady, G. T., 1978: The arrested topographic wave. *J. Phys. Oceanogr.,* **8,** 47–62, doi:10.1175/1520-0485(1978)008<0047:TATW>2.0.CO;2.

Fang, G., B. Zhao, and Y. Zhu, 1991: Water volume transport through the Taiwan Strait and the continental shelf of the East China Sea measured with current meters. *Oceanography of Asian Marginal Seas,* K. Takano, Ed., Elsevier, 345–358.

Guo, X., H. Hukuda, Y. Miyazawa, and T. Yamagata, 2003: A triply nested ocean model simulating the Kuroshio—Roles of horizontal resolution on JEBAR. *J. Phys. Oceanogr.,* **33,** 146–169, doi:10.1175/1520-0485(2003)033<0146:ATNOMF>2.0.CO;2.

Hyde, K. J. W., J. E. O'Reilly, and C. A. Oviatt, 2007: Validation of SeaWiFS chlorophyll *a* in Massachusetts Bay. *Cont. Shelf Res.,* **27,** 1677–1691, doi:10.1016/j.csr.2007.02.002.

Jan, S., D. D. Sheu, and H. M. Kuo, 2006: Water mass and throughflow transport variability in the Taiwan Strait. *J. Geophys. Res.,* **111,** C12012, doi:10.1029/2006JC003656.

Jordi, A., and D.-P. Wang, 2012: sbPOM: A parallel implementation of Princeton Ocean Model. *Environ. Modell. Software,* **39,** 58–61, doi:10.1016/j.envsoft.2012.05.013.

Kutzbach, J., 1967: Empirical eigenvectors of sea level pressure, surface temperature, and precipitation complexes over North America. *J. Appl. Meteor.,* **6,** 791–802, doi:10.1175/1520-0450(1967)006<0791:EEOSLP>2.0.CO;2.

Li, L., W. D. Nowlin Jr., and J. L. Su, 1998: Anticyclonic rings from the Kuroshio in the South China Sea. *Deep-Sea Res. I,* **45,** 1469–1482, doi:10.1016/S0967-0637(98)00026-0.

Lin, S. F., T. Y. Tang, S. Jan, and C.-J. Chen, 2005: Taiwan Strait Current in winter. *Cont. Shelf Res.,* **25,** 1023–1042, doi:10.1016/j.csr.2004.12.008.

Liu, K. K., T. Y. Tang, G. C. Gong, L. Y. Chen, and F. K. Shiah, 2000: Cross-shelf and along-shelf nutrient fluxes derived from

flow fields and chemical hydrography observed in the southern East China Sea off northern Taiwan. *Cont. Shelf Res.,* **20,** 493–523, doi:10.1016/S0278-4343(99)00083-7.

Mahadevan, A., E. D'Asaro, C. Lee, and M. J. Perry, 2012: Eddy-driven stratification initiates North Atlantic spring phytoplankton blooms. *Science,* **337,** 54–58, doi:10.1126/science.1218740.

Marshall, J., and R. A. Plumb, 2007: *Atmosphere, Ocean, and Climate Dynamics: An Introductory Text.* Elsevier Academic Press, 344 pp.

Mellor, G. L., S. Hakkinen, T. Ezer, and R. Patchen, 2002: A generalization of a sigma coordinate ocean model and an intercomparison of model vertical grids. *Ocean Forecasting: Conceptual Basis and Applications,* N. Pinardi and J. D. Woods, Eds., Springer, 55–72.

Mertz, G., and D. G. Wright, 1992: Interpretations of the JEBAR term. *J. Phys. Oceanogr.,* **22,** 301–305, doi:10.1175/1520-0485(1992)022<0301:IOTJT>2.0.CO;2.

Miyazawa, Y., and Coauthors, 2009: Water mass variability in the western North Pacific detected in a 15-year eddy resolving ocean reanalysis. *J. Oceanogr.,* **65,** 737–756, doi:10.1007/s10872-009-0063-3.

Nan, F., H. Xue, P. Xiu, F. Chai, M. Shi, and P. Guo, 2011: Oceanic eddy formation and propagation southwest of Taiwan. *J. Geophys. Res.,* **116,** C12045, doi:10.1029/2011JC007386.

Oey, L.-Y., Y.-L. Chang, Y.-C. Lin, M.-C. Chang, F.-H. Xu, and H.-F. Lu, 2013: ATOP—The Advanced Taiwan Ocean Prediction System based on the mpiPOM. Part 1: Model descriptions, analyses and results. *Terr. Atmos. Oceanic Sci.,* **24,** 137–158, doi:10.3319/TAO.2012.09.12.01(Oc).

——, ——, ——, ——, S. Varlamov, and Y. Miyazawa, 2014: Cross flows in the Taiwan Strait in winter. *J. Phys. Oceanogr.,* **44,** 801–817, doi:10.1175/JPO-D-13-0128.1.

O'Reilly, J. E., S. Maritorena, B. G. Mitchell, D. A. Siegel, K. L. Carder, S. A. Garver, M. Kahru, and C. McClain, 1998: Ocean color chlorophyll algorithms for SeaWiFS. *J. Geophys. Res.,* **103,** 24 937–24 953, doi:10.1029/98JC02160.

Shaw, P.-T., 1994: A numerical simulation of the evolution and propagation of Gulf Stream warm core rings. *J. Phys. Oceanogr.,* **24,** 573–586, doi:10.1175/1520-0485(1994)024<0573:ANSOTE>2.0.CO;2.

Sheu, W.-J., C.-R. Wu, and L.-Y. Oey, 2010: Blocking and westward passage of eddies in the Luzon Strait. *Deep-Sea Res. II,* **57,** 1783–1791, doi:10.1016/j.dsr2.2010.04.004.

Soeyanto, E., X. Guo, J. Ono, and Y. Miyazawa, 2014: Interannual variations of Kuroshio transport in the East China Sea and its relation to the Pacific decadal oscillation and mesoscale eddies. *J. Geophys. Res. Oceans,* **119,** 3595–3616, doi:10.1002/2013JC009529.

Tang, D. L., I.-H. Ni, F. E. Muller-Karger, and Z. J. Liu, 1998: Analysis of annual and spatial patterns of CZCS-derived concentration on the continental shelf of China. *Cont. Shelf Res.,* **18,** 1493–1515, doi:10.1016/S0278-4343(98)00039-9.

Volkov, D. L., T. Lee, and L.-L. Fu, 2008: Eddy-induced meridional heat transport in the ocean. *Geophys. Res. Lett.,* **35,** L20601, doi:10.1029/2008GL035490.

Wang, Y. H., S. Jan, and D. P. Wang, 2003: Transports and tidal current estimates in the Taiwan Strait from shipboard ADCP observations (1999–2001). *Estuarine Coastal Shelf Sci.,* **57,** 193–199, doi:10.1016/S0272-7714(02)00344-X.

Wu, C.-R., and Y.-C. Hsin, 2005: Volume transport through the Taiwan Strait: A numerical study. *Terr. Atmos. Oceanic Sci.,* **16,** 377–391.

——, S.-Y. Chao, and C. Hsu, 2007: Transient, seasonal and interannual variability of the Taiwan Strait Current. *J. Oceanogr.,* **63,** 821–833, doi:10.1007/s10872-007-0070-1.

Wyrtki, K., 1961: *Physical Oceanography of the Southeast Asian Waters.* NAGA Rep., Vol. 2, Scripps Institute of Oceanography, 195 pp.

Xu, F.-H., and L.-Y. Oey, 2011: The origin of along-shelf pressure gradient in the Middle Atlantic Bight. *J. Phys. Oceanogr.,* **41,** 1720–1740, doi:10.1175/2011JPO4589.1.

Yang, J., 2007: An oceanic current against the wind: How does Taiwan Island steer warm water into the East China Sea? *J. Phys. Oceanogr.,* **37,** 2563–2569, doi:10.1175/JPO3134.1.

Zhang, W.-Z., F. Chai, H.-S. Hong, and H. Xue, 2014: Volume transport through the Taiwan Strait and the effect of synoptic events. *Cont. Shelf Res.,* **88,** 117–125, doi:10.1016/j.csr.2014.07.010.

Zhang, Z., W. Wang, and B. Qiu, 2014: Oceanic mass transport by mesoscale eddies. *Science,* **345,** 322–324, doi:10.1126/science.1252418.